Herschel reveals a T_{dust}-unbiased selection of $z \sim 2$ ultraluminous infrared galaxies

G. E. Magdis,[1][*] D. Elbaz,[1] H. S. Hwang,[1] A. Amblard,[2] V. Arumugam,[3] H. Aussel,[1] A. Blain,[4] J. Bock,[4,5] A. Boselli,[6] V. Buat,[6] N. Castro-Rodríguez,[7,8] A. Cava,[7,8] P. Chanial,[9] D. L. Clements,[9] A. Conley,[10] L. Conversi,[11] A. Cooray,[2,4] C. D. Dowell,[4,5] E. Dwek,[12] S. Eales,[13] D. Farrah,[14] A. Franceschini,[15] J. Glenn,[10] M. Griffin,[13] M. Halpern,[16] E. Hatziminaoglou,[17] J. Huang,[18] E. Ibar,[19] K. Isaak,[13] E. Le Floc'h,[1] G. Lagache,[20] L. Levenson,[4,5] C. J. Lonsdale,[21] N. Lu,[4,22] S. Madden,[1] B. Maffei,[23] G. Mainetti,[15] L. Marchetti,[15] G. E. Morrison,[24,25] H. T. Nguyen,[4,5] B. O'Halloran,[9] S. J. Oliver,[14] A. Omont,[26] F. N. Owen,[27] M. J. Page,[28] M. Pannella,[27] P. Panuzzo,[1] A. Papageorgiou,[13] C. P. Pearson,[29,30] I. Pérez-Fournon,[7,8] M. Pohlen,[13] D. Rigopoulou,[29,31] D. Rizzo,[9] I. G. Roseboom,[14] M. Rowan-Robinson,[9] B. Schulz,[4,22] Douglas Scott,[16] N. Seymour,[28] D. L. Shupe,[4,22] A. J. Smith,[14] J. A. Stevens,[32] V. Strazzullo,[27] M. Symeonidis,[28] M. Trichas,[9] K. E. Tugwell,[28] M. Vaccari,[15] I. Valtchanov,[11] L. Vigroux,[26] L. Wang,[14] G. Wright,[19] C. K. Xu[4,22] and M. Zemcov[4,5]

[1]*Laboratoire AIM-Paris-Saclay, CEA/DSM/Irfu – CNRS – Université Paris Diderot, CE-Saclay, pt courrier 131, F-91191 Gif-sur-Yvette, France*
[2]*Department of Physics & Astronomy, University of California, Irvine, CA 92697, USA*
[3]*Institute for Astronomy, University of Edinburgh, Royal Observatory, Blackford Hill, Edinburgh EH9 3HJ*
[4]*California Institute of Technology, 1200 E. California Blvd, Pasadena, CA 91125, USA*
[5]*Jet Propulsion Laboratory, 4800 Oak Grove Drive, Pasadena, CA 91109, USA*
[6]*Laboratoire d'Astrophysique de Marseille, OAMP, Université Aix-marseille, CNRS, 38 rue Frédéric Joliot-Curie, 13388 Marseille cedex 13, France*
[7]*Instituto de Astrofísica de Canarias (IAC), E-38200 La Laguna, Tenerife, Spain*
[8]*Departamento de Astrofísica, Universidad de La Laguna (ULL), E-38205 La Laguna, Tenerife, Spain*
[9]*Astrophysics Group, Imperial College London, Blackett Laboratory, Prince Consort Road, London SW7 2AZ*
[10]*Department of Astrophysical and Planetary Sciences, CASA 389-UCB, University of Colorado, Boulder, CO 80309, USA*
[11]*Herschel Science Centre, European Space Astronomy Centre, Villanueva de la Cañada, 28691 Madrid, Spain*
[12]*Observational Cosmology Lab, Code 665, NASA Goddard Space Flight Center, Greenbelt, MD 20771, USA*
[13]*Cardiff School of Physics and Astronomy, Cardiff University, Queens Buildings, The Parade, Cardiff CF24 3AA*
[14]*Astronomy Centre, Department of Physics & Astronomy, University of Sussex, Brighton BN1 9QH*
[15]*Dipartimento di Astronomia, Università di Padova, vicolo Osservatorio, 3, 35122 Padova, Italy*
[16]*Department of Physics & Astronomy, University of British Columbia, 6224 Agricultural Road, Vancouver, BC V6T 1Z1, Canada*
[17]*ESO, Karl-Schwarzschild-Str. 2, 85748 Garching bei München, Germany*
[18]*Harvard-Smithsonian Center for Astrophysics, MS65, 60 Garden Street, Cambridge, MA 02138, USA*
[19]*UK Astronomy Technology Centre, Royal Observatory, Blackford Hill, Edinburgh EH9 3HJ*
[20]*Institut d'Astrophysique Spatiale (IAS), bâtiment 121, Université Paris-Sud 11 and CNRS (UMR 8617), 91405 Orsay, France*
[21]*National Radio Astronomy Observatory, 520 Edgemont Road, Charlottesville, VA 22903-2475, USA*
[22]*Infrared Processing and Analysis Center, MS 100-22, California Institute of Technology, JPL, Pasadena, CA 91125, USA*
[23]*School of Physics and Astronomy, The University of Manchester, Alan Turing Building, Oxford Road, Manchester M13 9PL*
[24]*Institute for Astronomy, University of Hawaii, Honolulu, HI 96822, USA*
[25]*Canada–France–Hawaii Telescope, Kamuela, HI 96743, USA*
[26]*Institut d'Astrophysique de Paris, UMR 7095, CNRS, UPMC Univ. Paris 06, 98bis boulevard Arago, F-75014 Paris, France*
[27]*National Radio Astronomy Observatory, 1003 Lopezville Road, Socorro, NM 87801, USA*
[28]*Mullard Space Science Laboratory, University College London, Holmbury St Mary, Dorking, Surrey RH5 6NT*
[29]*Space Science & Technology Department, Rutherford Appleton Laboratory, Chilton, Didcot, Oxfordshire OX11 0QX*
[30]*Institute for Space Imaging Science, University of Lethbridge, Lethbridge, Alberta T1K 3M4, Canada*
[31]*Department of Physics, University of Oxford, Keble Road, Oxford OX1 3RH*
[32]*Centre for Astrophysics Research, University of Hertfordshire, College Lane, Hatfield, Hertfordshire AL10 9AB*

[*]E-mail: georgios.magdis@cea.fr

ABSTRACT

Using *Herschel* Photodetector Array Camera (PACS) and Spectral and Photometric Imaging Receiver (SPIRE) observations of Lockman Hole-North and Great Observatories Origins Deep Survey-North (GOODS-N) as part of the *Herschel* Multi-tiered Extragalactic Survey (HerMES) project, we explore the far-infrared (IR) properties of a sample of mid-IR-selected starburst-dominated ultraluminous infrared galaxies (ULIRGs) at $z \sim 2$. The selection of the sample is based on the detection of the stellar bump that appears in the spectral energy distribution of star-forming galaxies at 1.6 μm. We derive robust estimates of infrared luminosities (L_{IR}) and dust temperatures (T_d) of the population and find that while the luminosities in our sample span less than an order of magnitude ($12.24 \leq \log(L_{IR}/L_{\odot}) \leq 12.94$), they cover a wide range of dust temperatures ($25 \leq T_d \leq 62$ K). Galaxies in our sample range from those that are as cold as high-z submillimetre galaxies (SMGs) to those that are as warm as optically faint radio galaxies (OFRGs) and local ULIRGs. Nevertheless, our sample has median $T_d = 42.3$ K, filling the gap between SMGs and OFRGs, bridging the two populations. We demonstrate that a significant fraction of our sample would be missed from ground-based (sub)mm surveys (850–1200 μm), showing that the latter introduce a bias towards the detection of colder sources. We conclude that *Herschel* observations confirm the existence of high-z ULIRGs warmer than SMGs, show that the mid-IR selection of high-z ULIRGs is not T_d dependent, reveal a large dispersion in T_d of high-z ULIRGs and provide the means to characterize the bulk of the ULIRG population, free from selection biases introduced by ground-based (sub)mm surveys.

Key words: galaxies: evolution – galaxies: high-redshift – galaxies: starburst – cosmology: observations – infrared: galaxies – submillimetre: galaxies.

1 INTRODUCTION

One of the most successful methods for selecting high-z ultraluminous infrared galaxies (ULIRGs; $L_{8-1000\,\mu m} > 10^{12}\,L_{\odot}$) is their direct far-infrared (IR) detection via ground-based (sub)millimetre surveys (e.g. Barger et al. 1998; Hughes et al. 1998; Mortier et al. 2005; Pope et al. 2006; Austermann et al. 2010). This technique has revealed the population of the so-called submillimetre galaxies (SMGs) that represent a significant class of high-z ULIRGs. Attempts to characterize their dust temperature (T_d) show that these galaxies are colder when compared to local ULIRGs (e.g. Chapman et al. 2005), suggesting that in general high-z ULIRGs tend to have lower dust temperatures. However, the submillimetre technique introduces a bias towards the selection of ULIRGs with lower dust temperatures while it misses warmer ULIRGs. First observational evidence of a missing population of high-redshift dusty star-forming galaxies with hotter dust has been given by Chapman et al. (2004) using a selection of radio-detected but submm-faint galaxies with ultraviolet (UV) spectra consistent with high-redshift starbursts. These optically faint radio galaxies (OFRGs) share similar properties with SMGs (e.g. stellar mass, star formation rate) but some have considerably higher dust temperatures (Casey et al. 2009; Magnelli et al. 2010).

Another technique that has been proven to pick high-z starburst-dominated ULIRGs efficiently is based on mid-IR colour selection. This technique relies on the detection of the rest-frame 1.6 μm bump in the spectral energy distribution (SED) of star-forming galaxies, produced by thermal emission from late-type stars and enhanced by an apparent emission feature due to H ions in the atmospheres of giant stars (Simpson & Eisenhardt 1999; Sawicki 2002). The advent of *Spitzer* allowed the detection of this feature in $z \sim 2$ galaxies and subsequent Infrared Spectrograph (IRS) spectroscopy

has demonstrated the efficiency of the method to select starburst-dominated ULIRGs in a redshift range of $1.5 < z < 2.5$ (e.g. Farrah et al. 2008; Weedman & Houck 2008; Huang et al. 2009). Further studies (Fiolet et al. 2009; Lonsdale et al. 2009; Kovács et al. 2010) indicate that only 40 per cent of their sample is made up of bright mm sources and thus belong to the class of SMGs, while most of the rest have lower $S_{1.2mm}$ fluxes.

The above suggests that a considerable fraction of mid-IR-selected high-z ULIRGs are missed by ground-based (sub)mm surveys. While this could naturally be explained if their dust temperature (for a given luminosity) is higher than that of the SMGs, this is not yet clear, as up to now the study of their far-IR properties is restricted to objects with ground (sub)mm detection or to the most luminous examples of the population with the highly confused BLAST beam (e.g. Dunlop et al. 2009; Ivison et al. 2010). Hence, a far-IR study of the population, free of the selection bias introduced by the ground-based submm detection, is required. Furthermore, detailed study of high-z ULIRGs is essential as up to now theoretical models fail to account for the inferred luminosities, star formation rates and number counts (Baugh et al. 2005; Dave et al. 2010).

In this study, we use observations of Lockman Hole-North (LHN) and Great Observatories Origins Deep Survey-North (GOODS-N) fields obtained by the *Herschel Space Observatory* (Pilbratt et al. 2010) as part of the *Herschel* Multi-tiered Extragalactic Survey (HerMES; Oliver et al. 2010), to investigate the far-IR properties of a sample of mid-IR-selected ULIRGs at $z \sim 2$ [Infrared Array Camera (IRAC) peakers]. Taking advantage of both the Photodetector Array Camera (PACS; Poglitsch et al. 2010) and the Spectral and Photometric Imaging Receiver (SPIRE; Griffin et al. 2010) data that probe the peak of the SED of galaxies at this redshift, we derive robust dust temperature measurements for the bulk of the population

and compare our sample to that of other high-z ULIRGs. Throughout this paper we assume $\Omega_m = 0.3$, $H_0 = 71\,\mathrm{km\,s^{-1}\,Mpc^{-1}}$ and $\Omega_\Lambda = 0.7$.

2 SAMPLE SELECTION AND *HERSCHEL* OBSERVATIONS

To select our sample we adopt the IRAC colour criteria introduced by Huang et al. (2009). In particular we search for galaxies in LHN that satisfy the following IRAC colour criteria: $0.05 < [3.6]-[4.5] < 0.4$ and $-0.7 < [3.6]-[8.0] < 0.5$ have $f_{24} > 0.2\,\mathrm{mJy}$ and $r_{\mathrm{vega}} > 23.0$ to avoid low-redshift interlopers. These criteria probe the 1.6-μm stellar bump while the red colour cuts ensure the rejection of power-law active galactic nuclei (AGNs). Subsequent IRS spectroscopy of ULIRGs selected with the above method has shown that this selection picks ULIRGs at very narrow redshift range $1.7 < z < 2.3$ with strong polycyclic aromatic hydrocarbon (PAH) features, indicative of intensive star formation (Huang et al. 2009).

We use the *Spitzer* Wide-Area Infrared Extragalactic Survey (SWIRE) multiwavelength catalogue (U, G, R, I, z, J, H, K+IRAC+MIPS; Strazzullo et al. 2010) over the 0.25 deg^2 of LHN covered by PACS and SPIRE, and we identify 32 objects that meet our criteria. We then match the sample with the joined *Herschel* PACS (100 and 160 μm) and SPIRE (250, 350 and 500 μm) XID catalogue (Roseboom et al. 2010). For the PACS data, where source confusion is less severe, we consider fluxes based on blind source extraction. For the SPIRE data we adopt the fluxes derived with source extraction based on 24-μm priors; we reject candidates with neighbouring ($d < 20\,\mathrm{arcsec}$) 24-μm sources whose f_{24} is >50 per cent that of our object. Finally, we require at least one PACS and SPIRE detection (3σ).

In the resulting LHN sample there are 25 candidate ULIRGs at $z \sim 2$, five of which have spectroscopic redshifts (Fiolet et al., in preparation). For the rest, we derive photometric redshifts, using the LEPHARE photo-z code (Ilbert et al. 2009). Namely, we fit the SED of the galaxies up to 8.0 μm with a wide range of template SEDs and consider dust attenuation that follows the prescription of Calzetti et al. (2000). For each object we adopt the redshift corresponding to the minimum χ^2 value of the fit. Two examples of the best-fitting template for two galaxies in our sample are depicted in Fig. 1. The uncertainty of the photometric redshifts was derived based on the

redshift probability distribution function (PDF(z)) and we choose to exclude from our analysis candidates with multiple solutions or uncertainties larger than $\Delta z = 0.5$. Furthermore, a comparison of the derived photometric redshifts with the spectroscopic redshifts that is available for five sources yields a very good agreement between the two values $\Delta z = (z_{\mathrm{photo}} - z_{\mathrm{spec}})/(1 + z_{\mathrm{spec}}) < 0.1$. The final LHN sample consists of 18 ULIRGs with median $z = 1.98$ and range $1.5 < z < 3.0$. Finally, we match this sample to the radio Very Large Array (VLA) 1.4 GHz catalogue of LHN (Owen & Morrison 2008).

To increase the size of our sample, we perform the same procedure in the GOODS-N field. Using the multiwavelength catalogue and the SPIRE data (PACS data for GOODS-N are not available for this study), we identify candidate ULIRGs with at least two detections (3σ) at SPIRE bands. To exclude sources with strong AGN activity, candidates with X-ray detection ($L_X[0.5–8.0\,\mathrm{keV}] > 3 \times 10^{42}\,\mathrm{erg\,s^{-1}}$) were removed. The final GOODS-N sample consists of seven sources. Out of these, one has a spectroscopic redshift ($z = 1.86$) while for the rest we adopt photometric redshifts by Le Borgne et al. (2009) (median $z = 1.83$ and $1.53 < z < 2.05$). The final combined sample (LHN and GOODS-N) consists of 25 ULIRGs with a median $z = 2.01$ and with 18 out of 25 objects lying in a narrow redshift range ($1.7 < z < 2.3$). PACS/SPIRE photometry of our sample is presented in Table 1, while IRAC, MIPS and mm and radio photometry is given in Table 2.

3 DERIVATION OF FAR-IR PROPERTIES

To derive estimates for the $L_{\mathrm{IR}}(L_{8-1000\,\mu\mathrm{m}})$ of the galaxies in our sample, we first convert their SED to rest frame applying k-corrections and then fit the PACS and SPIRE data with the libraries of Chary & Elbaz (2001, hereafter CE01) and Dale & Helou (2002). Results based on the two methods are in very close agreement indicating a median $L_{\mathrm{IR}} = 3 \times 10^{12}\,\mathrm{L_\odot}$. The CE01-derived L_{IR} values for each object are summarized in Table 1, while examples of the rest-frame SEDs along with the best-fitting CE01 templates for two ULIRGs in our sample are shown in Fig. 1.

To derive the dust temperature of galaxies in our sample, we use a single temperature modified blackbody fitting form in which the thermal dust spectrum is approximated as $F_\nu \propto \nu^{3+\beta}/(e^{(h\nu/kT_\mathrm{d})} - 1)$. This model was fitted to *Herschel* data with rest frame $\lambda > 40\,\mu$m,
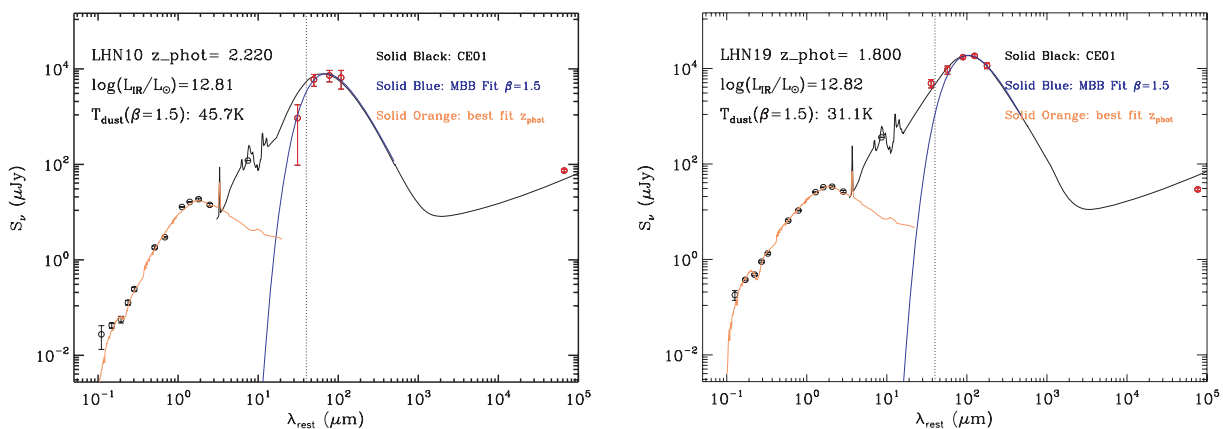

Figure 1. Rest-frame SEDs and derivation of the far-IR properties for two ULIRGs in our sample (divided by $1 + z$ for illustrative purposes). The solid orange line shows the best-fitting template up to observed 8 μm as derived by LEPHARE photo-z code. The solid black line shows the best-fitting CE01 model while the blue line depicts the best-fitting modified blackbody (with $\beta = 1.5$), used to derive T_d estimates. The vertical dotted line indicates the wavelength cut, below which photometric data were not considered in the modified blackbody fit. Red circles denote *Herschel* data.

Table 1. Far-IR properties of mid-IR-selected $z \sim 2$ ULIRGs.

ID	z	$S_{100}{}^a$ (mJy)	$S_{160}{}^a$ (mJy)	S_{250} (mJy)	S_{350} (mJy)	S_{500} (mJy)	L_{IR} (L$_\odot$)	T_d (K)
LHN0	2.01[b]	7.36 ± 3.67	23.04 ± 4.99	27.17 ± 1.94	13.20 ± 1.77	4.76 ± 2.81	12.70 ± 0.16	51.61 ± 2.26
LHN1	1.95[b]	13.37 ± 2.50	41.78 ± 5.96	52.51 ± 2.14	34.21 ± 2.86	5.02 ± 5.67	12.99 ± 0.10	44.43 ± 1.24
LHN2	2.01	5.12 ± 1.68	0.00 ± 0.00	7.36 ± 1.57	6.01 ± 1.74	0.53 ± 1.97	12.25 ± 0.32	38.66 ± 4.47
LHN3	2.40	8.94 ± 2.80	0.00 ± 0.00	15.11 ± 1.71	15.20 ± 2.12	14.93 ± 2.38	12.57 ± 0.05	33.20 ± 0.72
LHN4	1.72	20.05 ± 2.83	35.52 ± 6.37	32.53 ± 7.87	10.83 ± 15.04	0.00 ± 0.00	12.81 ± 0.11	46.64 ± 2.30
LHN5	1.98	8.70 ± 2.59	0.00 ± 0.00	16.86 ± 1.64	13.12 ± 1.95	7.07 ± 2.23	12.52 ± 0.15	40.00 ± 4.25
LHN8	2.07[b]	11.07 ± 2.53	46.10 ± 5.23	46.65 ± 2.03	41.73 ± 1.67	17.70 ± 2.19	12.92 ± 0.10	42.30 ± 1.04
LHN10	2.22	3.01 ± 2.70	19.29 ± 5.36	23.60 ± 6.40	21.09 ± 8.92	0.00 ± 0.00	12.86 ± 0.16	45.74 ± 3.12
LHN11	2.09	6.18 ± 2.01	0.00 ± 0.00	13.87 ± 2.07	14.70 ± 2.40	0.00 ± 0.00	12.50 ± 0.18	32.70 ± 0.36
LHN16	2.10[b]	5.47 ± 2.74	13.44 ± 4.41	29.35 ± 6.31	37.53 ± 8.47	0.00 ± 0.00	12.57 ± 0.20	44.11 ± 4.83
LHN19	1.80	13.65 ± 2.69	26.41 ± 5.18	48.44 ± 2.54	51.48 ± 3.34	32.11 ± 4.38	12.72 ± 0.09	31.14 ± 0.42
LHN20	1.64	6.48 ± 2.86	13.90 ± 4.39	13.16 ± 1.63	5.65 ± 1.68	0.00 ± 0.00	12.35 ± 0.24	50.81 ± 4.78
LHN24	2.15	2.82 ± 4.05	21.95 ± 6.87	16.57 ± 1.77	15.74 ± 2.11	12.31 ± 3.81	12.68 ± 0.15	38.64 ± 3.64
LHN25	2.18	4.55 ± 2.42	13.87 ± 4.21	14.60 ± 3.38	3.42 ± 3.83	9.82 ± 2.13	12.56 ± 0.26	38.82 ± 3.61
LHN27	2.23	5.23 ± 3.44	18.90 ± 4.68	15.47 ± 2.44	10.34 ± 2.39	12.49 s ± 3.57	12.61 ± 0.28	52.00 ± 0.68
LHN29	1.96[b]	0.00 ± 0.00	12.83 ± 4.11	27.47 ± 1.75	32.45 ± 2.74	18.45 ± 3.80	12.51 ± 0.19	30.51 ± 1.34
LHN30	1.56	9.53 ± 2.82	22.48 ± 5.10	20.80 ± 2.00	11.37 ± 1.62	0.00 ± 0.00	12.43 ± 0.18	45.75 ± 2.43
LHN31	3.03	5.38 ± 2.79	12.77 ± 4.22	21.98 ± 1.61	14.76 ± 2.51	0.00 ± 0.0	12.94 ± 0.17	62.10 ± 5.87
GN18	2.05	–	–	9.46 ± 1.09	11.72 ± 1.62	0.00 ± 0.00	12.38 ± 0.14	30.46 ± 2.44
GN32	1.83	–	–	41.36 ± 1.02	41.46 ± 1.62	0.00 ± 0.00	12.72 ± 0.14	35.70 ± 2.86
GN34	1.83	–	–	15.12 ± 1.37	13.64 ± 2.10	0.00 ± 0.00	12.28 ± 0.14	35.44 ± 2.83
GN35	1.83	–	–	37.47 ± 2.04	32.22 ± 4.45	0.00 ± 0.00	12.69 ± 0.14	39.82 ± 3.19
GN44	1.74	–	–	13.51 ± 1.55	16.18 ± 2.65	0.00 ± 0.00	12.24 ± 0.13	34.46 ± 2.76
GN46	1.66	–	–	41.45 ± 1.45	52.20 ± 2.06	26.40 ± 4.24	12.71 ± 0.14	36.13 ± 2.89
GN58	1.52	–	–	23.59 ± 1.07	12.59 ± 2.05	0.00 ± 0.00	12.41 ± 0.14	44.58 ± 3.57

[a] No available PACS data for GOODS-N in this study.

[b] IRS spectroscopy by Fiolet et al. (2010).

Table 2. Summary of ancillary data.

ID	RA	Dec.	$S_{3.6}$ (μJy)	$S_{4.5}$ (μJy)	$S_{5.8}$ (μJy)	$S_{8.0}$ (μJy)	S_{24} (μJy)	$S_{1.4\,GHz}$ (μJy)
LHN0	161.127548	58.921799	41.3 ± 0.8	49.5 ± 1.1	55.3 ± 4.0	53.9 ± 3.8	781 ± 24.0	101.7 ± 14.2
LHN1	161.487091	58.888611	26.4 ± 0.7	33.6 ± 1.0	39.5 ± 3.6	36.9 ± 3.6	684 ± 24.1	314.8 ± 19.1
LHN2	161.376022	58.920658	28.4 ± 0.7	34.2 ± 0.7	40.2 ± 3.5	27.1 ± 2.6	375 ± 22.3	29.0 ± 7.5
LHN3	161.415726	58.906940	30.9 ± 0.6	39.5 ± 0.9	47.2 ± 3.2	47.8 ± 3.0	485 ± 24.1	46.9 ± 4.3
LHN4	161.545685	58.879189	52.9 ± 0.9	66.9 ± 1.1	57.0 ± 3.6	52.1 ± 3.4	401 ± 25.0	160.2 ± 10.7
LHN5	161.160263	59.075150	32.3 ± 0.6	37.8 ± 0.9	30.0 ± 3.1	33.5 ± 3.4	375 ± 23.3	51.3 ± 9.8
LHN8	161.661163	58.936852	29.5 ± 0.7	38.8 ± 1.0	58.2 ± 3.7	42.0 ± 3.5	662 ± 23.4	159.5 ± 9.9
LHN10	161.525223	59.141270	45.4 ± 0.7	58.0 ± 1.0	60.2 ± 3.0	45.7 ± 3.2	194 ± 25.6	238.9 ± 16.2
LHN11	161.231583	59.167912	48.9 ± 0.8	59.0 ± 1.1	54.4 ± 3.3	36.0 ± 3.3	258 ± 24.8	45.1 ± 10.0
LHN16	161.824844	59.042171	35.8 ± 0.8	50.0 ± 1.1	77.4 ± 4.0	52.1 ± 3.8	567 ± 26.4	55.1 ± 5.4
LHN19	161.507462	59.154690	72.1 ± 1.0	91.3 ± 1.5	93.5 ± 3.9	74.0 ± 3.9	1011 ± 23.1	82.2 ± 5.7
LHN20	161.676163	59.069839	53.2 ± 0.8	61.6 ± 1.2	57.3 ± 3.3	42.9 ± 3.5	307 ± 23.9	70.6 ± 5.0
LHN24	161.843964	59.019981	31.9 ± 0.6	41.0 ± 1.0	41.1 ± 3.1	38.0 ± 3.3	439 ± 23.3	73.7 ± 9.4
LHN25	161.933746	59.106892	36.3 ± 0.5	43.5 ± 0.8	46.8 ± 2.8	36.9 ± 3.3	656 ± 25.7	54.9 ± 13.7
LHN27	161.729813	59.191101	28.9 ± 0.6	36.8 ± 0.7	40.0 ± 3.5	38.4 ± 3.0	337 ± 22.5	36.4 ± 10.5
LHN29	161.909683	59.169449	44.4 ± 0.6	51.0 ± 0.8	52.3 ± 3.1	47.7 ± 3.3	688 ± 24.0	69.2 ± 9.3
LHN30	161.944641	59.257740	50.5 ± 0.6	59.4 ± 0.9	40.0 ± 2.9	50.3 ± 3.3	341 ± 23.4	87.6 ± 16.8
LHN31	161.935730	59.210369	35.8 ± 0.6	44.5 ± 0.9	39.5 ± 3.1	35.8 ± 3.4	404 ± 21.8	0.0 ± 0.0
GN18	189.262684	62.142494	11.4 ± 0.1	13.9 ± 0.1	10.3 ± 0.5	13.3 ± 0.6	230 ± 7.2	–
GN32	189.256739	62.196195	53.9 ± 0.1	70.1 ± 0.1	8.8 ± 0.3	57.9 ± 0.4	716 ± 8.1	–
GN34	189.399541	62.345261	29.3 ± 0.1	37.5 ± 0.1	25.3 ± 0.5	28.2 ± 0.5	178 ± 5.4	–
GN35	189.076657	62.264067	14.7 ± 0.1	19.6 ± 0.1	22.2 ± 0.4	20.4 ± 0.4	314 ± 5.3	–
GN44	189.074144	62.235591	49.2 ± 0.1	55.6 ± 0.1	35.9 ± 0.4	40.2 ± 0.5	428 ± 7.2	–
GN46	189.297273	62.225206	37.9 ± 0.1	45.0 ± 0.1	14.8 ± 0.3	37.8 ± 0.4	534 ± 8.6	–
GN58	189.294242	62.376245	38.7 ± 0.1	47.9 ± 0.1	12.4 ± 0.7	46.4 ± 0.6	383 ± 4.6	–

assuming a fixed emissivity index of $\beta = 1.5$. This wavelength cut was introduced to avoid fitting emission from very small grains (VSGs). The T_d of each object was obtained from the best-fitting model, based on the minimization of the χ^2 value. The uncertainty for each T_d value was estimated by repeating the same procedure for random perturbations of the fitted photometric points within their errors (following a normal distribution). The best-fitting model for two ULIRGs in our sample is shown in Fig. 1 (solid blue line)

with the T_d for each of the galaxies summarized in Table 1. Finally, to check whether the lack of PACS data for the GOODS-N sample introduces any systematic bias in the derived properties we repeated the fitting procedure for the LHN sample, excluding this time the PACS photometric points. The values derived with and without the PACS were in good agreement ($\langle \Delta T_d \rangle = 1.9$ K).

3.1 AGN contribution to our sample

It has been shown by previous studies that the selection criteria of our sample have been very successful in selecting starburst over AGN-dominated ULIRGs (e.g. Farrah et al. 2008; Huang et al. 2009). Indeed, for five ULIRGs in LHN, IRS spectroscopy indicates that their mid-IR emission is dominated by vigorous star formation rather than an AGN (Fiolet et al., in preparation). None of our objects in this field is detected by *Chandra* to a 0.3–2.5 keV flux limit of 5×10^{-16} erg cm^{-2} s^{-1} ($L_X > 8.5 \times 10^{42}$ erg s^{-1} for $z = 2.0$; Polletta et al. 2006), while on construction of the GOODS-N sample all candidate objects with X-ray detection at a flux limit of 1.95×10^{-17} erg cm^{-2} s^{-1} were rejected from our analysis. As the moderate depth of the LHN X-ray data do not provide strong constraints on the AGN contribution we further explore this issue by the q parameter ($q = \log[L_{40-120 \mu m}/(3.75 \times 10^{12}$ W)] $- \log[L_{1.4 GHz}/(W Hz^{-1})]$; Helou, Soifer & Rowan-Robinson 1985). Given that almost all of our galaxies have radio detections, we estimate the q parameter and find a mean $\langle q \rangle = 2.21$ with intrinsic dispersion $\sigma_q = 0.17$. This is in agreement with that found by Younger et al. (2009) and the q of star-forming galaxies, quoted by Ivison et al. (2010) ($q = 2.40$, $2\sigma_q = 0.27$). These considerations support the conclusion of Huang et al. (2009) that an AGN contributes little (<10–20 per cent) to the bolometric luminosity of these objects.

4 RESULTS

4.1 Far-IR properties and comparison with other ULIRG samples

Galaxies in our sample have dust temperatures that span a wide range $25 \leq T_d \leq 62$ (K), while their luminosities vary by less than an order of magnitude $12.24 \leq \log(L_{IR}/L_\odot) \leq 12.94$. The median values are $T_d = 42.3$ K and $L_{IR} = 3 \times 10^{12} L_\odot$, indicating a star formation rate of ~520 M$_\odot$ yr^{-1} [assuming a Salpeter initial mass function (IMF)]. It is interesting to compare these values to those of ULIRG samples selected by different techniques.

We consider a large set of $z \sim 2$ SMGs (Chapman et al. 2005; Kovacs et al. 2006), a sample of $z \sim 2$ OFRGs (Casey et al. 2009) and a compilation of local/intermediate-z ($0 < z < 0.98$) ULIRGs (Farrah et al. 2003; Yang et al. 2007; Clements, Dunne & Eales 2010). In all these studies, the method to derive T_d estimates is similar to ours, fitting modified blackbody models to the far-IR photometric points. For studies that quote L_{FIR} instead of L_{IR} we adopt the following conversion factor between the two values: $L_{IR} = 1.4 \times L_{FIR}$ (Dale et al. 2001). We note that preliminary results by Hwang et al. (in preparation), Chapman et al. (in preparation) and Chanial et al. (in preparation) indicate that the far-IR properties of SMGs and OFRGs, when *Herschel* data are taken into account, are, in general, consistent with the results obtained in the pre-*Herschel* era.

In Fig. 2, we show the L_{IR}–T_d relation for our sample as compared to that of local/intermediate-z ULIRGs, SMGs and OFRGs. For the luminosity bin of our sample, SMGs have a median $T_d = 36 \pm 8$ K while OFRGs are considerably warmer with median $T_d = 47 \pm$
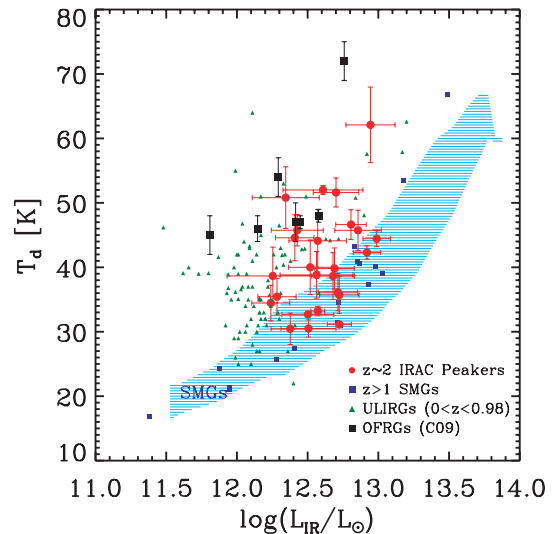

Figure 2. The L_{IR}–T_d relation for our sample (red circles). Included are results for local/intermediate-z ULIRGs (green filled triangles; Farrah et al. 2003; Yang et al. 2007; Clements et al. 2010), high-z SMGs (blue squares; Chapman et al. 2005; Kovacs et al. 2006) and OFRGs (black squares; Casey et al. 2009). The cyan shaded area denotes the 2σ envelope of the L_{IR}–T_d relation of high-z SMGs. For a given L_{IR}, our sample spans a wide range of dust temperatures, bridging the 'cold' high-z SMGs to the 'warmer' local/intermediate-z ULIRGs and $z \sim 2$ OFRGs.

3 K (Magnelli et al. 2010) and dust temperatures similar to that of local ULIRGs. Therefore, it appears that the two methods select ULIRGs with significantly different dust temperatures, and with no significant overlap between them. Taking advantage of the wealth of multiwavelength data in GOODS-N, we find that a large fraction of SMGs (15/24) and OFRGs (4/5) in GOODS-N (Pope et al. 2006; Casey et al. 2009) that fall in the redshift bin (1.5 < z < 3.0) of our sample satisfy the IRAC-peakers colour criteria, if we relax the f_{24} cut.

Based on this plot there are a number of significant results to be drawn. First of all, our observations confirm the existence of ULIRGs in the high-z Universe with dust temperature higher than that of SMGs. Furthermore, it seems that the selection of high-z ULIRGs based on the detection of the 1.6-μm bump does not favour a particular T_d, selecting ULIRGs that overlap with the SMGs and OFRGs but also ULIRGs of intermediate T_d. Indeed, we see that objects in our sample range from those that are as cold as SMGs to objects as warm as OFRGs, while a significant fraction lies in the intermediate region between the two samples, bridging the two populations. We also note that a large fraction of the sample falls in the T_d–L_{IR} relation of the local ULIRGs. Finally, our data indicate that the T_d dispersion of high-z ULIRGs is larger than that of the local ULIRGs as derived based on *IRAS* observations. This discrepancy mainly arises due to the absence of cold sources in the local Universe, although the *IRAS* selection might miss existing cold sources, introducing a bias towards warmer ULIRGs.

4.2 SMGs: evidence of selection bias towards colder ULIRGs

There is growing evidence that ground-based (sub)mm observations introduce a systematic bias towards the detection of cold ULIRGs. As mentioned above this was first discussed by Chapman et al. (2004), introducing the populations of OFRGs, while a similar conclusion was reached recently by Chapin et al. (2010) using BLAST
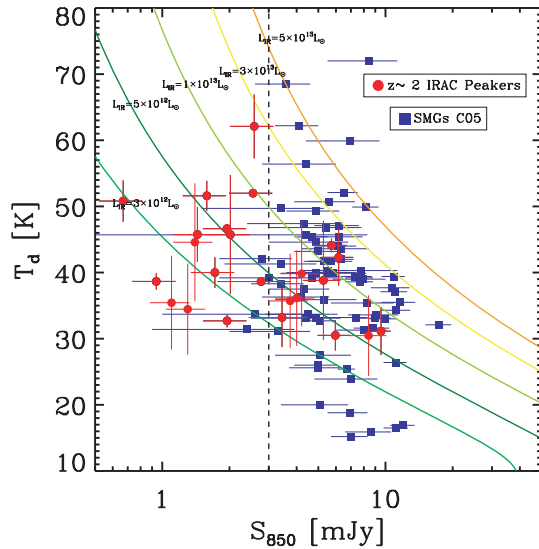
Figure 3. Dust temperature versus the estimated S_{850} flux densities of galaxies in our sample (red circles). We also include T_d measurements and observed S_{850} flux densities of high-z SMGs by Chapman et al. (2005) (blue squares). Solid lines represent tracks in constant L_{IR} while the vertical dotted line indicates the confusion limit of current ground-based submm surveys. It is evident that a significant fraction of our sample lies below the detection limit and would be missed by the SCUBA 850 μm surveys, if we consider that the detection limit should be above the confusion.

data. In Fig. 2, we showed that a fraction of IRAC peakers also tends to be warmer than high-z SMGs. We now ask whether these IRAC peakers would be missed by the submm selection.

To investigate this, we estimate the S_{850} flux densities of our sample based on the best-fitting CE01 model that was obtained through the fitting of the *Herschel* photometric points. The predicted S_{850} fluxes of our sample along with the measured submm flux of high-z SMGs are plotted over the derived T_d of the two populations in Fig. 3. We also overplot tracks in constant L_{IR}. This plot illustrates that a significant fraction (~60 per cent) of the mid-IR-selected ULIRGs in our sample have S_{850} flux densities lower than that of the SMGs, lie below the confusion limit at 850 μm (2–3 mJy; Knudsen, van der Werf & Kneib 2008) and hence would be missed by ground-based (sub)mm surveys. Nevertheless, we also find IRAC peakers with predicted S_{850} above the detection limit and which therefore should be detected in the submm. Indeed, four of our objects in LNH (LHN1, LHN8, LHN16 and LHN29) have been detected [signal-to-noise ratio (S/N) > 3] by the Max Planck Millimetre Bolometer array (MAMBO) 1.2 mm (Fiolet et al. 2009; Kovács et al. 2010). For these objects we use the formula described by Ivison et al. (2005) to convert the observed 1.2 mm to 850 μm flux densities and then compare these values with the predicted S_{850} flux densities that we derived from our analysis. The two values are in close agreement for all objects, with a median difference of 0.15 mJy. Furthermore, we find that all galaxies in our sample with MAMBO observations but no detection (LHN0, LHN19, LHN25; Fiolet et al. 2009) have predicted fluxes below the detection limit. The same test for the GOODS-N sample reveals that our analysis successfully predicts the submm fluxes of two objects with Submillimeter Common User Bolometer Array (SCUBA) 850-μm detection (GN17, GN06; Borys et al. 2005; Pope et al. 2006).

Another way to explore this issue is a direct visualization of the SEDs of the sources. Such an approach is free of systematics and uncertainties of SED fitting that could possibly affect/bias our re-
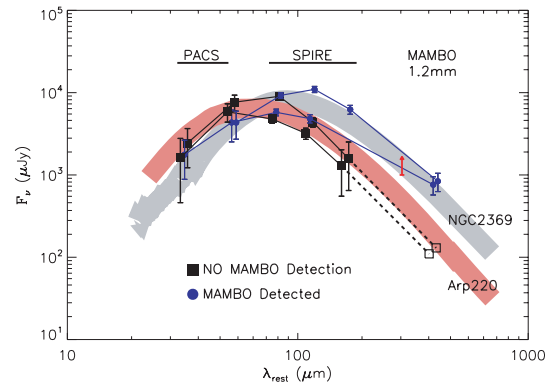

Figure 4. The far-IR part of the SED of two MAMBO-detected (blue circles) and two MAMBO-undetected sources (black squares) from our sample (divided by $1 + z$). All four sources are chosen to have comparable L_{IR} and f_{250}. The far-IR part of the SED of Arp 220 (coral shaded area) and that of NGC 2369 (grey shaded area) are also shown. For the MAMBO-undetected sources the open boxes correspond to the 1.2-mm flux density based on the SED extrapolation. The red arrow indicates the confusion limit of 850-μm surveys. The SED of MAMBO-undetected sources peaks at shorter wavelengths, indicating warmer T_d and lower 850–1200 μm emission when compared to that of IRAM-detected sources. This plot illustrates that among sources with comparable L_{IR} those with higher T_d are missed by current ground-based surveys.

sults. In Fig. 4, we show the far-IR SED of four sources in LHN that have been followed up by MAMBO 1.2-mm observations. Two sources are not detected at 1.2 mm while the other two have a >3σ detection. These sources are also chosen to have similar L_{IR}(12.5 < log($L_{IR}/L_\odot$) < 12.7) and similar fluxes at 250 μm. It is evident that for the same luminosity, the far-IR SED of the MAMBO-undetected sources peaks at shorter wavelengths compared to that of the MAMBO-detected sources. This indicates a clear difference of the dust temperature and subsequently of the 850–1200 μm emission of the two samples, with MAMBO-undetected sources having warmer T_d and considerably lower 850–1200 μm flux densities.

Recently, Kovács et al. (2010) presented a far-IR study of 20 luminous $z \sim 2$ mid-IR-selected starbursts based on SHARC-2 350 μm and concluded that their properties are indistinguishable from the purely SMG population. Although this seems to contradict our findings, this is not the case. Since their study focuses on IRAC peakers with $S_{1.2\,mm}$ > 2 mJy, their sample is biased towards the most submm luminous galaxies among the mid-IR-selected ULIRGs and hence those that are likely to share similar properties with the SMGs. As illustrated in Fig. 3 such galaxies exist in our sample too. In fact, our sample shares four objects in common with that of Kovács et al. (2010) for which the estimates of the far-IR properties between the two studies are in very good agreement (Table 3). On the other hand, as we have shown above, due to the requirement of

Table 3. SHARC 350-μm and MAMBO 1.2-mm flux densities of our LHN sample.

ID	S (350 μm)[a] (mJy)	S (1.2 mm)[b] (mJy)
LHN1	39.7 ± 5.9	3.08 ± 0.58
LHN8	31.9 ± 4.9	2.13 ± 0.71
LHN16	49.7 ± 6.5	2.66 ± 0.78
LHN29	31.8 ± 5.9	2.48 ± 0.74

[a]Flux densities by Kovács et al. (2010).
[b]Flux densities by Fiolet et al. (2009).

MAMBO detection, they miss a large fraction of mid-IR-selected ULIRGs that have faint 850–1200 μm flux densities and their properties are different from those of SMGs. Furthermore, although there are no 850–1200 μm observations for some galaxies in our sample, the fraction of galaxies with predicted S_{850} above the detection limit is consistent with the fraction of MAMBO-detected mid-IR ULIRGs (∼40 per cent) in the study of Lonsdale et al. (2009) and Fiolet et al. (2009). To summarize, *Herschel* data allow us for the first time to characterize the far-IR properties of ∼50 per cent of the mid-IR-selected ULIRGs that would be missed by ground-based (sub)mm surveys and reveal that their properties are different from those of SCUBA/IRAM-selected galaxies.

5 CONCLUSIONS

We have presented the far-IR properties of mid-IR-selected ULIRGs at $z \sim 2$ in LHN and GOODS-N fields, based on *Herschel* PACS and SPIRE observations. We showed that for a narrow range of luminosities, our sample spans a wide range of T_d, indicating that the mid-IR selection of high-z ULIRGs does not introduce a systematic bias in T_d. Sources in our sample range from those that are as cold as high-z SMGs to objects as warm as OFRGs, while a significant fraction has intermediate T_d, bridging the two populations. We also demonstrated that a significant fraction of our sample would be missed from (sub)mm surveys, showing that the submm technique introduces a bias towards the detection of colder ULIRG sources. We confirmed the existence of star-forming ULIRGs at high-z that are warmer than SMGs and showed that the T_d dispersion at high-z is larger than that found in the local Universe. While this large dispersion in T_d suggests a diversity of the physical mechanisms that drive the star formation activity in the early galaxies, its origin remains unclear. *Herschel* observations of larger samples in the rest of the HerMES survey will address this question as well as the contribution of ULIRGs to the star formation density and their clustering properties.

REFERENCES

Austermann J. E. et al., 2010, MNRAS, 401, 160
Barger A. J., Cowie L. L., Sanders D. B., Fulton E., Taniguchi Y., Sato Y., Kawara K., Okuda H., 1998, Nat, 394, 248
Baugh C. M., Lacey C. G., Frenk C. S., Granato G. L., Silva L., Bressan A., Benson A. J., Cole S., 2005, MNRAS, 356, 1191
Borys C., Smail I., Chapman S. C., Blain A. W., Alexander D. M., Ivison R. J., 2005, ApJ, 635, 253
Calzetti D., Armus L., Bohlin R. C., Kinney A. L., Koornneef J., Storchi-Bergmann T., 2000, ApJ, 533, 682
Casey C. M. et al., 2009, MNRAS, 399, 121
Chapin E. L. et al., 2010, preprint (arXiv:1003.2647)
Chapman S. C., Smail I., Blain A. W., Ivison R. J., 2004, ApJ, 614, 671
Chapman S. C., Blain A. W., Smail I., Ivison R. J., 2005, ApJ, 622, 772
Chary R., Elbaz D., 2001, ApJ, 556, 562 (CE01)
Clements D. L., Dunne L., Eales S., 2010, MNRAS, 403, 274
Dale D. A., Helou G., 2002, ApJ, 576, 159
Dale D., Helou G., Contursi A., Silbermann N. A., Kolhatkar S., 2001, ApJ, 549, 215
Dave R., Finlator K., Oppenheimer B. D., Fardal M., Katz N., Keres D., Weinberg D. H., 2010, MNRAS, 404, 1355
Dunlop J. S. et al., 2009, preprint (arXiv:0910.3642)
Farrah D., Afonso J., Efstathiou A., Rowan-Robinson M., Fox M., Clements D., 2003, MNRAS, 343, 585
Farrah D. et al., 2008, ApJ, 677, 957
Fiolet N. et al., 2009, A&A, 508, 117
Griffin M. J. et al., 2010, A&A, 518, 3
Helou G., Soifer B. T., Rowan-Robinson M., 1985, ApJ, 298, 7
Huang J.-S. et al., 2009, ApJ, 700, 183
Hughes D. H. et al., 1998, Nat, 394, 241
Ilbert O. et al., 2009, ApJ, 690, 1236
Ivison R. J. et al., 2005, MNRAS, 364, 1025
Ivison R. J. et al., 2010, MNRAS, 402, 245
Knudsen K. K., van der Werf P. P., Kneib J.-P., 2008, MNRAS, 384, 1611
Kovacs A., Chapman S. C., Dowell C. D., Blain A. W., Ivison R. J., Smail I., Phillips T. G., 2006, ApJ, 650, 592
Kovács A. et al., 2010, ApJ, 717, 29
Le Borgne D., Elbaz D., Ocvirk P., Pichon L., 2009, A&A, 504, 727
Lonsdale C. J. et al., 2009, ApJ, 692, 422
Magnelli B. et al., 2010, A&A, 518, 28
Mortier A. M. J. et al., 2005, MNRAS, 363, 563
Oliver S. et al., 2010, A&A, 518, 21
Owen F. N., Morrison G. E., 2008, AJ, 136, 1889
Pilbratt G. L. et al., 2010, A&A, 518, 1
Poglitsch A. et al., 2010, A&A, 518, 2
Polletta M. et al., 2006, ApJ, 642, 673
Pope A. et al., 2006, MNRAS, 370, 1185
Roseboom I. J. et al., 2010, MNRAS, in press (this issue, arXiv:1009.1658, doi:10.1111/j.1365-2966.2010.17634.x)
Sawicki M., 2002, AJ, 124, 3050
Simpson C., Eisenhardt P., 1999, PASP, 111, 691
Strazzullo V. et al., 2010, ApJ, 714, 1305
Weedman D. W., Houck J. R., 2008, ApJ, 686, 127
Yang M., Greve T. R., Dowell C. D., Borys C., 2007, ApJ, 660, 1198
Younger J. D. et al., 2009, MNRAS, 394, 1685

This paper has been typeset from a TeX/LaTeX file prepared by the author.